nanomaterials

MDPI

Article

Spherical $Bi_2WO_6/Bi_2S_3/MoS_2$ n-p Heterojunction with Excellent Visible-Light Photocatalytic Reduction Cr(VI) Activity

Jing Ren, Tingting Hu, Qinghua Gong, Qian Wang, Bin Sun *, Tingting Gao, Pei Cao and Guowei Zhou *

Key Laboratory of Fine Chemicals in Universities of Shandong, School of Chemistry and Chemical Engineering, Qilu University of Technology (Shandong Academy of Sciences), Jinan 250353, China; 17862963042@163.com (J.R.); hutingting_1981@163.com (T.H.); 18396814931@163.com (Q.G.); qianwang0510@126.com (Q.W.); ttgao@qlu.edu.cn (T.G.); caopei8956@126.com (P.C.)

* Correspondence: binsun@qlu.edu.cn (B.S.); gwzhou@qlu.edu.cn or guoweizhou@hotmail.com (G.Z.); Tel.: +86-0531-8963-1696 (G.Z.)

Received: 9 August 2020; Accepted: 8 September 2020; Published: 11 September 2020

Abstract: Exploiting excellent photocatalytic activity and stable heterostructure composites are of critical importance for environmental sustainability. The spherical $Bi_2WO_6/Bi_2S_3/MoS_2$ n-p heterojunction is first prepared via an in situ hydrothermal method using Bi_2WO_6, $Na_2MoO_4{\cdot}2H_2O$, and CH_4N_2S, in which the intermediate phase Bi_2S_3 is formed due to chemical coupling interaction of Bi_2WO_6 and CH_4N_2S. Scanning electron microscopy indicates that the compactness of the sample can be easily adjusted by changing the contents of S and Mo sources in the solution. The results of ultraviolet–visible (UV–vis) diffuse reflectance spectra, photoluminescence, transient photocurrent response, and electrochemical impedance spectra indicate that the formation of heterojunctions contributes to enhancing visible-light utilization and promoting photogenerated carrier separation and transfer. The composite material is used as a catalyst for the visible light photocatalytic reduction of Cr(VI). Remarkably, the optimal $Bi_2WO_6/Bi_2S_3/MoS_2$ n-p heterojunction achieves the greatest Cr(VI) reduction rate of 100% within 75 min (λ > 420 nm, pH = 2); this rate is considerably better than the Cr(VI) reduction rate of pure Bi_2WO_6. The recycling experiment also reveals that the photocatalytic performance of the n-p heterojunction toward Cr(VI) is still maintained at 80% after three cycles, indicating that the n-p heterojunction has excellent structural stability. The capture experiment proves that the main active species in the system are electrons. The reasonable mechanism of $Bi_2WO_6/Bi_2S_3/MoS_2$ photocatalytic reduction Cr(VI) is proposed. Our work provides new research ideas for the design of ternary heterojunction composites and new strategies for the development of photocatalysts for wastewater treatment.

Keywords: n-p heterojunction; $Bi_2WO_6/Bi_2S_3/MoS_2$; Visible-light; Photocatalytic reduction; Cr(VI)

1. Introduction

With the rapid development of industrial production, the pollution of water and land resources by heavy metals is becoming increasingly serious [1–3]. Water-soluble, non-biodegradable hexavalent chromium Cr(VI), which easily penetrates through food chain enrichment, can induce cellular oxidative stress, leading to DNA damage, gene mutation, fetal malformation, and carcinogenesis, is one of the most dangerous heavy metals [4,5]. Cr(VI) is widely applied in smelting, electroplating, painting, chemical manufacturing, and tanned leather [6–8]. The World Health Organization stipulates that the maximum limit of pollutants in surface water is 0.1 mg L^{-1}. However, the concentration of Cr(VI) in sewage is usually higher than 100 mg L^{-1} [9]. Therefore, the development of economical and efficient

wastewater chromium removal technology is significant. At present, the methods for reducing the Cr(VI) concentration in aqueous solutions mainly include electrochemical precipitation, ion exchange, membrane filtration, photocatalytic degradation, and adsorption [10–14]. The reduction of Cr(VI) to less toxic Cr(III) by semiconductor photocatalytic technology is considered an effective, low-cost method that generates no harmful substances [15–17].

Bismuth-based photocatalysts have always been a research hotspot in the field of photocatalysis. Bismuth tungstate (Bi_2WO_6) has been widely studied for its safety, cheap, proper band gap (~2.8 eV), high stability, and excellent photocatalytic activity [18–20]. However, bare Bi_2WO_6 has the disadvantages of high photo-generated electron-holes recombination efficiency, narrow light absorption range, small specific surface area, and weak surface adsorption capacity, which makes it exhibit poor photocatalytic performance [21–23]. Therefore, a scientific strategy that enhances the performance of photocatalysts in practical applications must be developed.

At present, the methods used to improve the photocatalytic activity of semiconductors are as follows: nanostructure modification [24], surface engineering, and homojunction/heterostructure construction. Among these methods, the construction of heterojunctions is considered the most simple and efficient [25–27]. The reason is that the establishment of heterojunction cannot only effectively broaden the range of light response and enhance the light absorption of catalyst but also achieve the effective separation of photo-generated carriers under the action of internal electric field and improve the catalytic activity [28,29]. Many Bi_2WO_6-based heterojunction photocatalysts, such as Bi_2WO_6/MoS_2 [30], Bi_2WO_6/Fe_2O_3 [25], Bi_2WO_6/Bi_2S_3 [31], CdS/Bi/Bi_2WO_6 [32], meso-tetra (4-carboxyphenyl) porphyrin/rGO/Bi_2WO_6 [33], and Co_3O_4/Ag/Bi_2WO_6 [34], have been used to improve the performance of pure Bi_2WO_6. Huang et al. successfully prepared a new flower-shaped AgBr/Bi_2WO_6 catalyst, which showed good catalytic performance in the degradation of tetracycline (TC) under visible light (vis-light) irradiation [35]. Wan et al. prepared Au/Bi_2WO_6–MoS_2 heterojunction photocatalysts, which exhibited excellent vis-light photocatalytic activity in Cr(VI) and tetracycline hydrochloride degradation [23]. Xue et al. synthesized new g-C_3N_4/Bi_2WO_6/AgI catalyst by a hierarchical assembly method. Compared with bare Bi_2WO_6, the ternary heterojunction composite has stronger redox capacity and exhibits better catalytic activity during the photodegradation of organic pollutants such as TC [36]. Long et al. prepared 3D flower-like MoS_2/Bi_2S_3 heterostructures with excellent photocatalytic activity toward the photodegradation of low concentrations of organic pollutants [37]. The above results show that the successful construction of multi-component heterostructure can effectively improve the photocatalytic activity compared with a single component. However, the Bi_2WO_6-based photocatalysts still have disadvantages, including a complex preparation method, narrow light response range, and rapid photogenerated charge carrier recombination. In recent years, the use of MoS_2 and Bi_2S_3 coupled with other semiconductors for boosted photocatalytic performance has been widely investigated. To our knowledge, the preparation and application in photocatalysis of the $Bi_2WO_6/Bi_2S_3/MoS_2$ ternary heterojunction has not been reported. Hence, seeking a facile and controllable preparation method to fabricate ternary heterojunctions containing Bi_2WO_6, Bi_2S_3, and MoS_2 is of great importance for improving the photocatalytic performance of Bi_2WO_6 in environmental purification.

Based on the above considerations, in the present work, $Bi_2WO_6/Bi_2S_3/MoS_2$ heterojunction ternary composite materials are prepared via hydrothermal method using the synthesized Bi_2WO_6 microspheres as substrate (Scheme 1) and which are used for photocatalytic reduction of Cr(VI) to Cr(III). Importantly, the formation of Bi_2S_3 does not require an additional Bi source, and S^{2-} partially replaces WO_6^{6-} in Bi_2WO_6. This process maintains a superior spherical structure and is beneficial to the uniform distribution of Bi_2S_3 in the composite. The compactness of composite nanoflakes can be easily adjusted by changing the content of sodium molybdate dihydrate ($Na_2MoO_4 \cdot 2H_2O$) and thiourea (CH_4N_2S) in the solution during the hydrothermal process. To the best of our knowledge, the $Bi_2WO_6/Bi_2S_3/MoS_2$ heterojunction for Cr(VI) photocatalytic reduction under vis-light irradiation is investigated for the first time. The composites have higher adsorption capacity and photocatalytic activity than pure Bi_2WO_6 in

terms of Cr(VI) reduction due to the successful construction of heterojunction structure. The synergistic effect among the three components enhances light absorption and realizes the effective separation and transmission of photogenerated carriers. The Cr(VI) reduction rate of $Bi_2WO_6/Bi_2S_3/MoS_2$ reaches 100% within 75 min (λ > 420 nm, pH = 2) and is considerably better than that of the pure Bi_2WO_6. These results provide new research ideas for the design of ternary heterojunctions to develop highly efficient vis-light-driven photocatalysts for wastewater treatment.

Scheme 1. Schematic diagram of preparing $Bi_2WO_6/Bi_2S_3/MoS_2$ heterojunction ternary composites.

2. Experimental Section

2.1. Materials and Chemicals

All chemicals and materials in this work were of analytical grade and purchased from commercial suppliers, which could be directly utilized without any further purification. Sodium tungstate dihydrate ($Na_2WO_4{\cdot}2H_2O$, AR, 99.5%), $Na_2MoO_4{\cdot}2H_2O$ (AR, 99.0%), bismuth(III) nitrate pentahydrate ($Bi(NO_3)_3{\cdot}5H_2O$, AR, 99.0%), and CH_4N_2S (AR, 99.0%) were acquired from Sigma-Aldrich (St. Louis, MO, USA). Absolute ethanol (C_2H_5OH, AR, ≥99.7%), glacial acetic acid (CH_3COOH, AR, ≥99.5%), polyvinyl pyrrolidone K30 (PVP K30, AR), and other chemicals used in the experiments were bought from Shanghai Chemical Reagent Co., Ltd. (Shanghai, China). Ultrapure water (18.2 MΩ cm^{-1}) was served throughout the study and acquired from the Milli-Q water purifying system (Millipore Corp., Bedford, MA, USA).

2.2. Synthesis of Spherical Bi_2WO_6 Nanostructures

Solutions A and B were prepared in the synthesis of Bi_2WO_6 precursor. In solution A, 2 mmol $Bi(NO_3)_3{\cdot}5H_2O$ and 4 g PVP K30 were added to a mixed solution of 50 mL ultrapure water, absolute ethanol, and glacial acetic acid with a 3:1:1 volume ratio and then stirred at room temperature for 60 min. In solution B, 1 mmol $Na_2WO_4{\cdot}2H_2O$ was added to 20 mL H_2O for 30 min of ultrasonication. After the solutions were clarified, solution B was dropped to solution A under agitation and stirred continuously for 60 min to obtain a white uniform suspension. The suspension was transferred to a Teflon-sealed autoclave (100 mL) for a solvothermal reaction at 180 °C for 18 h. After cooling, the light-yellow product was collected, washed thrice with absolute ethanol and ultrapure water in sequence, and finally dried overnight and ground for reserves.

2.3. Synthesis of $Bi_2WO_6/Bi_2S_3/MoS_2$ n-p Heterojunction Photocatalyst

$Bi_2WO_6/Bi_2S_3/MoS_2$ n-p heterojunction nanocomposites were prepared by a simple hydrothermal reaction. First, 200 mg Bi_2WO_6 was dispersed in 40 mL water with ultrasonic treatment for 10 min. Further 1 h stirring treatment was needed after the addition of 200 mg $Na_2MoO_4{\cdot}2H_2O$ and 400 mg CH_4N_2S as an ion source. Second, the dispersion was transferred to 100 mL Teflon-sealed autoclave for hydrothermal reaction at 200 °C for 24 h. Wait for cooling, the obtained sample (named as product BBM-3) was rinsed with ultrapure water and anhydrous ethanol for thrice and then dried overnight at 60 °C in a vacuum oven. As a control, the addition amount of $Na_2MoO_4{\cdot}2H_2O$:CH_4N_2S was adjusted (80 mg:160 mg, 120 mg:240 mg, 300 mg:600 mg), and the corresponding products with BBM-1, BBM-2,

and BBM-4 were expressed. In addition, the preparation method of pure MoS_2 nanosheets was similar to the above process except that Bi_2WO_6 was not added.

2.4. Characterization

Powder X-ray diffraction (XRD) patterns were obtained on a SmartLab SE X-ray diffractometer (Rigaku Corp., Tokyo, Japan) with Cu Kα (λ = 1.5046 Å) radiation. Raman spectra were measured using a Renishaw in Via9 Raman microscope system (Renishaw, London, UK) with a 50× objective and a 532 nm laser irradiation to focal point the laser beam into a spot with a diameter of approximately 1 μm. The morphology and energy-dispersive spectra (EDS) of the samples were tested and characterized by a field-emission scanning electron microscope (FESEM, Regulus 8220, Hitachi, Tokyo, Japan). The microstructure and lattice fringe of the samples were examined by a transmission electron microscope (TEM, JEM-2100, JEOL, Tokyo, Japan) and high-resolution TEM (HRTEM, JEM-2100). The elemental composition and chemical state of the samples were determined by X-ray photoelectron spectroscopy (XPS) (Perkin-Elmer PHI5300 spectrometer, Perkin Elmer, Waltham, MA, USA). The specific surface areas of the samples were obtained based on the N_2 adsorption–desorption isotherm tested on a Micromeritics ASAP 2460 system (ASAP, Norcross, GA, USA). The ultraviolet–visible (UV–vis) diffuse reflectance spectra (DRS) were tested within a 200 nm to 800 nm wavelength range using a spectrometer (UV-2600, Shimadzu, Kyoto, Japan) with $BaSO_4$ as a reference. A Hitachi F4500 fluorescence spectrophotometer (Hitachi, Tokyo, Japan) was used to test the photoluminescence (PL) measurements ($\lambda_{excitation}$ = 300 nm). The Mott–Schottky curves, electrochemical impedance spectra (EIS), and photocurrent response experiments were carried out using the electrochemical workstation (PARSTAT 4000, Ametec, Berwyn, PA, USA) with a conventional three-electrode configuration (working electrode: fluorine-doped tin oxide conducting glass; counter electrode: platinum plate; reference electrode: Ag/AgCl electrode) and Na_2SO_4 aqueous solution as the electrolyte (0.1 mol L^{-1}).

2.5. Photocatalytic Activity Experiments

The specific operational steps of the prefabricated catalysts for photocatalytic reduction of Cr(VI) (Cr(VI) source: $K_2Cr_2O_7$) were as follows: Cr(VI) solution with concentration of 40 mg L^{-1} was prepared using ultrapure water as solvent. Then, 50 mL of this initial solution was accurately measured and placed in the reaction vessel. Next, the initial solution pH to 2 was adjusted with HCl solution (1 mol L^{-1}). Afterward, the 20 mg as-synthesized catalysts were evenly dispersed in the solution by ultrasonication. Before vis-light irradiation, the suspension was stored in the dark place and stirred for 60 min to reach equilibrium of adsorption and desorption. Under the irradiation by Xe lamp (300 W, 100 mW cm^{-2}, $\lambda > 420$ nm), 3 mL suspension was taken out in the reaction container every 15 min and centrifuged (9000 r min^{-1}, 10 min). Then, the supernatant was collected with microporous (0.22 μm) membrane filter syringe to eliminate residual particles. NaOH (1 mol L^{-1}) or HCl (1 mol L^{-1}) solution was used to adjust the pH of Cr(VI) solution to investigate the effect of solution pH on photocatalysis. Finally, the Cr(VI) concentration was obtained by measuring the absorbance of the supernatant at 540 nm (UV-2600, Shimadzu) with diphenylcarbazide approach (Electronic Supplementary Materials).

3. Results and Discussion

3.1. X-ray Diffraction (XRD) and Raman Analysis

Figure 1a shows the XRD patterns of the products. For Bi_2WO_6, the diffraction peaks at 2θ = 28.3°, 32.8°, 47.1°, 56.0°, 58.5°, 68.8°, 76.1°, and 78.5° correspond to the (131), (200), (202), (133), (262), (400), (2102), and (204) crystal faces of the Bi_2WO_6 orthorhombic phase (JCPDS Card No.39-0256), respectively [38,39]. The three diffraction peaks of bare MoS_2 at 9.0°, 32.0°, and 58.0° correspond to the (002), (100), and (110) crystal faces of 2H-MoS_2, respectively. The peaks at 9.0° and 17.0° indicate the formation of a layered structure with enlarged interlayer spacing [40]. For heterojunction

photocatalysts, the XRD patterns display new diffraction peaks. The diffraction peaks located at 25.0° correspond to the (130) crystal plane of Bi_2S_3 [41]. Given the strong interaction force between Bi^{3+} and S^{2-}, Bi_2S_3 will be formed at relatively high temperatures [42]. The $Bi_2WO_6/Bi_2S_3/MoS_2$ samples show a discernible peak at approximately 32.0°, which is attributed to the (100) crystal plane of MoS_2, indicating that the composite material contains MoS_2 component. However, the absence of the highest MoS_2 intensity peak (~9.0°) from the heterostructure samples indicates that MoS_2 nanosheets may contain only a few layers that are too thin to be detected by XRD [43].

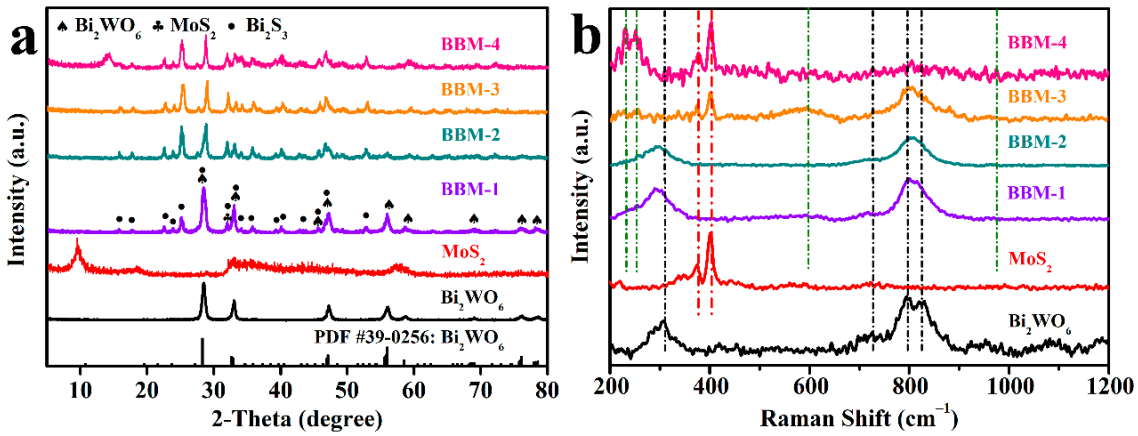

Figure 1. X-ray diffraction (XRD) patterns (**a**), and Raman spectra (**b**) of bare Bi_2WO_6, MoS_2, BBM-1, BBM-2, BBM-3, and BBM-4 heterojunction.

Raman measurements of the as-synthesized samples were performed in the range of 200–1200 cm^{-1}, and the results are shown in Figure 1b. The black, green, and red dashed lines in the figure represent the Raman characteristic peaks of Bi_2WO_6, Bi_2S_3, and MoS_2, respectively. The peaks of 308, 723, 798, and 829 cm^{-1} in the Raman spectra are characteristic Raman shifts of Bi_2WO_6 [44]. The Raman peaks of Bi_2S_3 are located at 234.8, 260, 590, and 970 cm^{-1}, of which the peaks at 234.8 and 260 cm^{-1} matched the A_g^1 and B_{1g} vibration mode, respectively [45]. Meanwhile, the typical peaks at 383 and 408 cm^{-1} are ascribed to the E^1_{2g} and A_{1g} vibrations of MoS_2, respectively [42,45]. Based on the above results, the $Bi_2WO_6/Bi_2S_3/MoS_2$ ternary composites are successfully prepared.

3.2. Morphology

As shown in the scanning electron microscope (SEM) images (Figure 2a), Bi_2WO_6 microspheres with diameters of 2.6–3.0 μm are self-assembled from nanosheets. The SEM images in Figure 2b–e show that the degree of looseness of the $Bi_2WO_6/Bi_2S_3/MoS_2$ microsphere increases accordingly with the increase in Mo and S sources concentration during the hydrothermal process. Nevertheless, with the further increase in concentration, MoS_2 agglomerates are formed on the $Bi_2WO_6/Bi_2S_3/MoS_2$ surface, and the corresponding results are shown in Figure 2e. This finding is consistent with the information expressed in the TEM diagram in Figure 2f–j. The causes of these phenomenon are as follows: I. A strong affinity exists between Bi^{3+} and S^{2-}, which reacts under high temperature and pressure to form Bi_2S_3 ($Bi_2WO_6 + 3S^{2-} \rightarrow Bi_2S_3 + WO_6^{6-}$) [42,45]. II. Bi_2WO_6 is consumed during this process, and Bi_2S_3 and MoS_2 are generated. As the consumption of Bi_2WO_6 increases, the structure becomes looser. III. The formation of MoS_2 agglomerates is mainly caused by the excessively high concentration of Mo and S sources, which promotes the nucleation speed to extreme degrees [46]. Soon afterward, BBM-3 is used as the model, and its composition is characterized by high-resolution transmission electron microscopy (HRTEM). Figure 2k shows the tight interface between Bi_2WO_6, Bi_2S_3, and MoS_2 in the BBM-3. The measured interplanar distances of 0.315, 0.360, and 0.620 nm belong to the (131) crystal plane of orthorhombic Bi_2WO_6, the (130) plane of Bi_2S_3, and the (002) lattice plane of MoS_2, respectively [47–49]. The high-magnification TEM of BBM-3 (Figure S1), which can intuitively illustrate

the close interface contact between Bi_2WO_6, Bi_2S_3, and MoS_2, confirms the successful construction of the $Bi_2WO_6/Bi_2S_3/MoS_2$ heterojunction [42]. Meanwhile, element mapping is used to analyze BBM-3 in depth to further determine the distribution of Mo, S, Bi, W, and O in the material. The results (Figure 2l–p) coincide with the EDS characterization results (Figure S2), confirming that BBM-3 consists of Mo, S, Bi, W, and O. The above results confirm that $Bi_2WO_6/Bi_2S_3/MoS_2$ n-p heterojunction with spherical structure can be synthesized by a simple in-situ hydrothermal method.

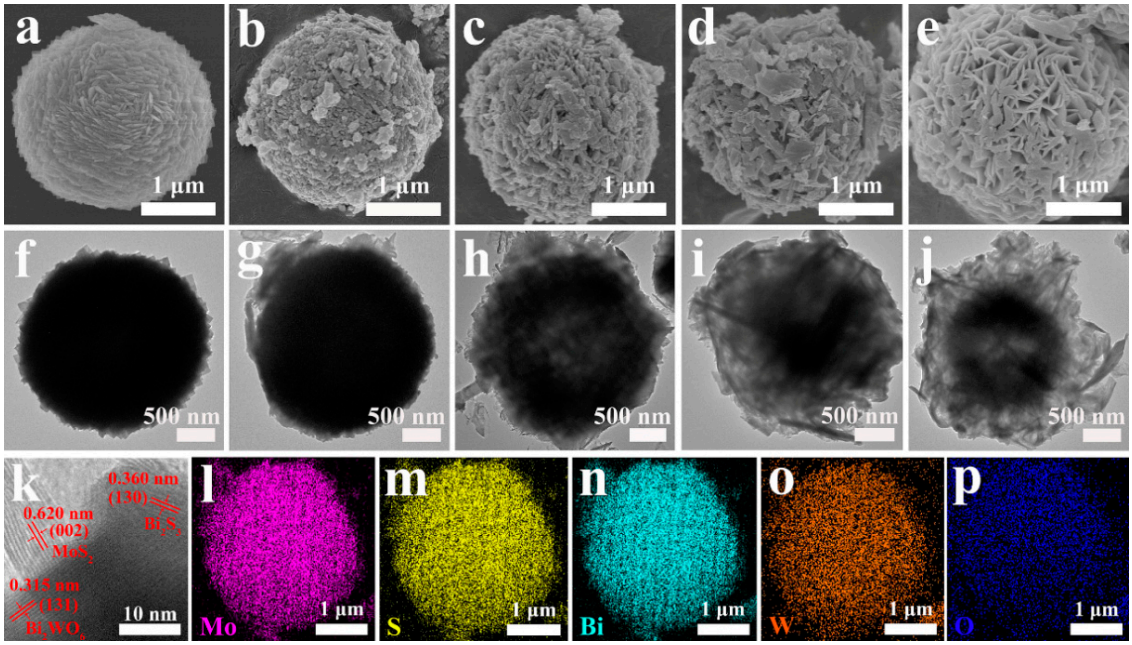

Figure 2. Scanning electron microscope (SEM) and transmission electron microscope (TEM) images of (**a**,**f**) bare Bi_2WO_6, (**b**,**g**) BBM-1, (**c**,**h**) BBM-2, (**d**,**i**) BBM-3, and (**e**,**j**) BBM-4. High-resolution TEM (HRTEM) image (**k**), and energy-dispersive spectra (EDS) mapping images (**l**–**p**) of BBM-3.

3.3. X-ray Photoelectron Spectroscopy (XPS) Analysis

The survey XPS curves in Figure 3a indicate that BBM-3 is composed of Mo, Bi, S, W, and O. Figure 3b–e shows the high-resolution spectra of Mo 3d, Bi 4f, W 4f, and O1s, respectively. The Mo 3d (Figure 3b) shows two peaks centered at 227.6 and 230.8 eV, which correspond to Mo $3d_{5/2}$ and Mo $3d_{3/2}$ of Mo^{4+}, respectively [50]. The satellite peak at approximately 234.7 eV represents Mo^{6+} [51]. In addition, the mid-strong peak at 225.4 eV can be well matched to S 2s [50]. The characteristic signal in Bi 4f diagram (Figure 3c) is formed by Bi $4f_{7/2}$ at 157.4 eV, Bi $4f_{5/2}$ at 162.7 eV, and S 2p at 160.6 eV [52]. The difference between the binding energy of Bi $4f_{7/2}$ and Bi $4f_{5/2}$ is 5.3 eV, indicating that Bi exists in BBM-3 as Bi^{3+}. Figure 3d contains the peaks at 35.2 and 37.6 eV, which are characteristics of W $4f_{7/2}$ and W $4f_{5/2}$, respectively [53]. The three fitted peaks in the O 1s spectrum (Figure 3e) are located at 531.5, 530.6, and 529.7 eV, which indicates that three types of O are present in BBM-3. The peak at 531.5 eV represents the chemically adsorbed oxygen (O–H) on the surface of BBM-3, whereas the peaks at 530.6 and 529.7 eV correspond to the O–Bi and O–W lattice oxygen in BBM-3, respectively [54]. Compared with the peaks of pure Bi_2WO_6, Bi_2S_3, and MoS_2, the Mo 3d and Bi 4f peaks of BBM-3 display a shift ~1.0 eV to the lower binding energy direction. Conversely, the W 4f peak of BBM-3 shows a shift ~1.0 eV to the higher binding energy direction. These results are primarily due to strong interactions and charge transfer among Bi_2WO_6, Bi_2S_3, and MoS_2 in BBM-3 (Figure S3) [29]. The above XPS analyses confirm again that Bi_2WO_6, Bi_2S_3, and MoS_2 coexist in the $Bi_2WO_6/Bi_2S_3/MoS_2$ ternary heterojunction photocatalyst.

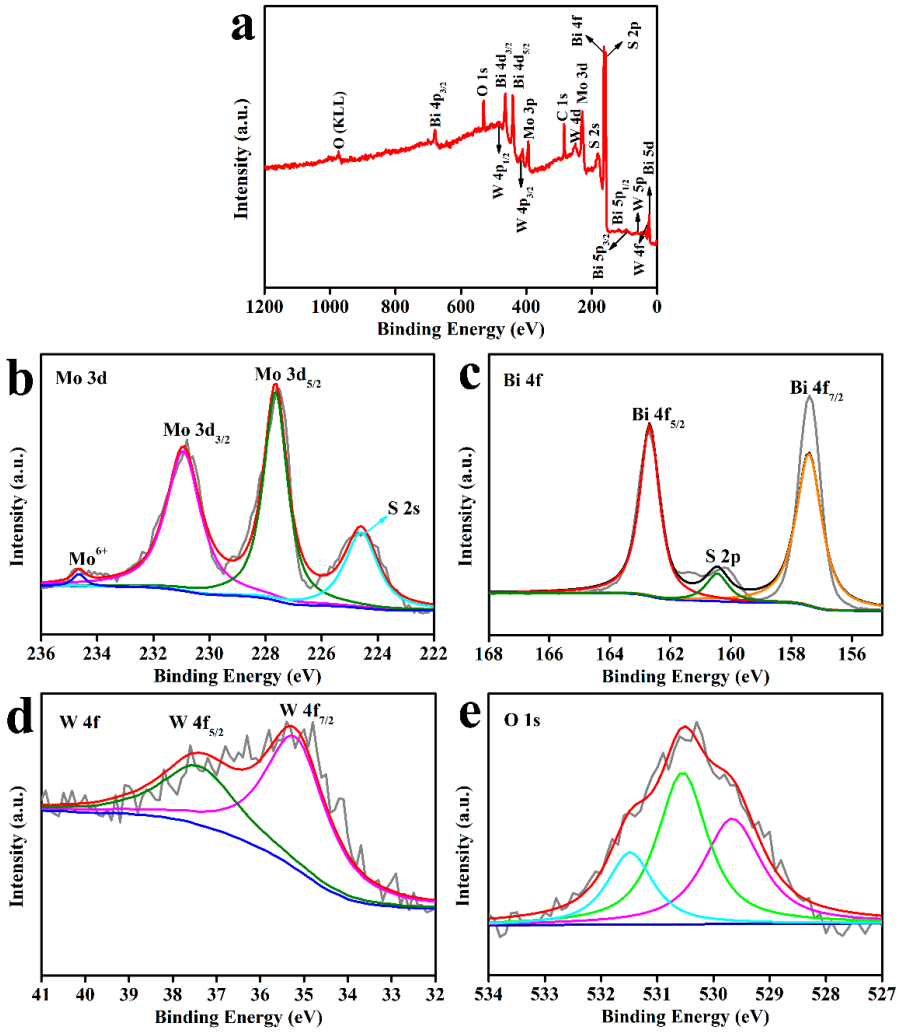

Figure 3. X-ray photoelectron spectroscopy (XPS) analysis of BBM-3 showing (**a**) survey, (**b**) Mo 3d, (**c**) Bi 4f, (**d**) W 4f, and (**e**) O 1s spectra.

3.4. Brunauer–Emmett–Teller (BET) Specific Surface Area Analysis

As shown in Figure S4, the Bi_2WO_6 and $Bi_2WO_6/Bi_2S_3/MoS_2$ ternary heterojunction samples exhibit type IV isotherms, which indicate the existence of mesoporous structures [11,22]. The Brunauer–Emmett–Teller (BET) surface area of $Bi_2WO_6/Bi_2S_3/MoS_2$ composites is higher than that of bare Bi_2WO_6 (14.7 m^2 g^{-1}). The BET surface areas of BBM-1, BBM-2, BBM-3, and BBM-4 are 16.6, 19.7, 22.7, and 19.4 m^2 g^{-1}, respectively. Compared with pure Bi_2WO_6, $Bi_2WO_6/Bi_2S_3/MoS_2$ composites have high BET surface areas and rich mesoporous structures, which facilitate the adsorption and reduction of Cr(VI).

3.5. Ultraviolet–Visible (UV–Vis) Absorption and Band Gap Positions

The DRS of the pristine Bi_2WO_6, pristine MoS_2, and ternary composites are recorded to investigate the light absorption of the samples. As shown in Figure 4a, for the pristine Bi_2WO_6, its intrinsic light absorption edge is at 450 nm, which means that the material has light absorption only in the UV and partially visible regions. By contrast, pure MoS_2 shows a strong absorption in the UV–vis region. As expected, $Bi_2WO_6/Bi_2S_3/MoS_2$ ternary heterojunction photocatalyst extends the vis-light absorption range compared with the Bi_2WO_6. Thus, the good photocatalysis performance of the composite is

predicted. Furthermore, the bandgap energy (E_g) of as-fabricated materials is obtained in accordance with Tauc's equation (Equation (1)) [44,55]:

$$(\alpha h\nu) = A(h\nu - E_g)^{n/2}, \quad (1)$$

where α: absorption coefficient, h: Planck's constant, ν: light frequency, and A: a constant.

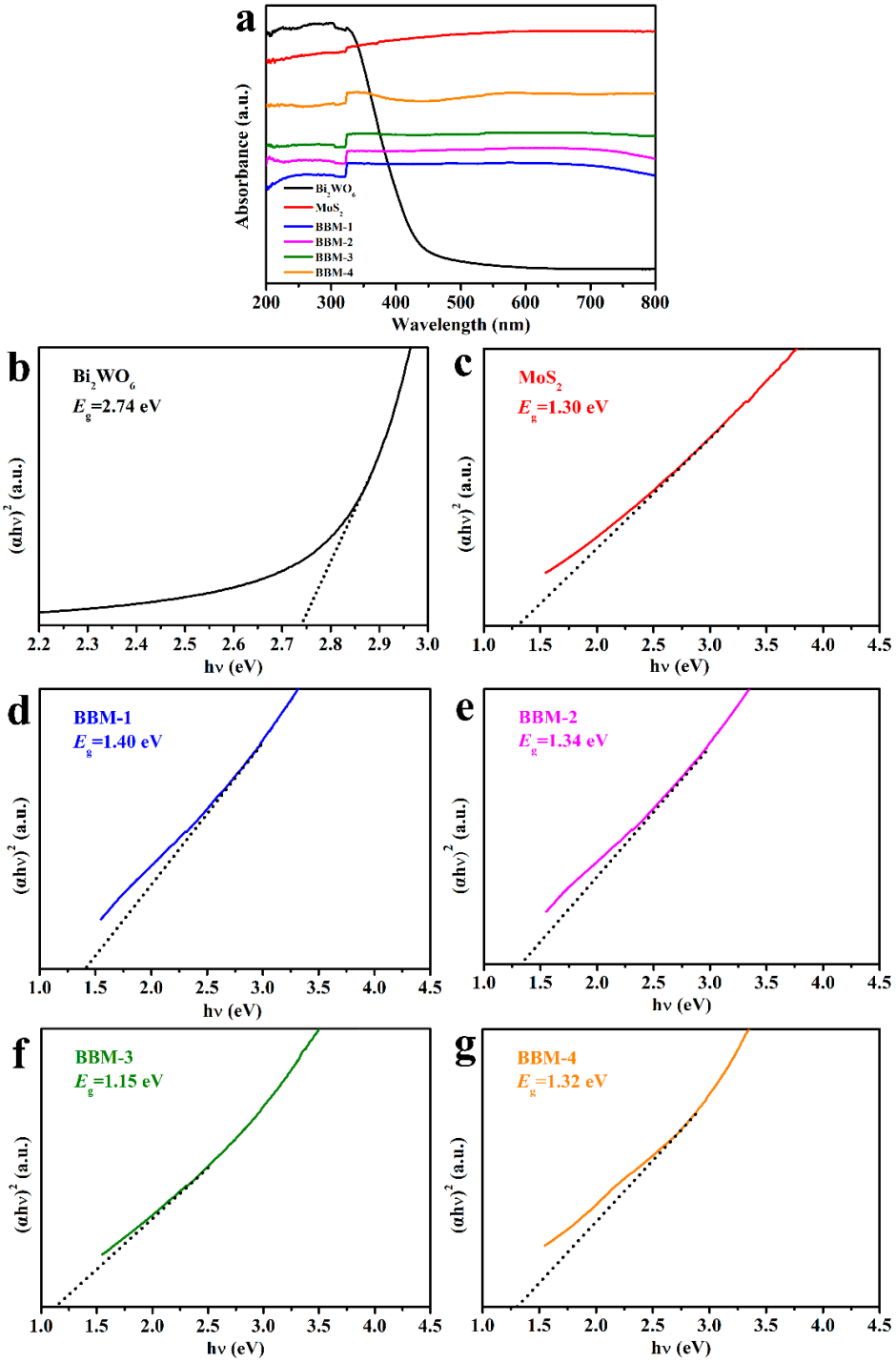

Figure 4. (**a**) Ultraviolet–visible (UV–vis) diffuse reflectance spectra (DRS) spectra of Bi_2WO_6, MoS_2, BBM-1, BBM-2, BBM-3, and BBM-4. (**b**–**g**) Plot of $(\alpha h\nu)^2$ versus photon energy of Bi_2WO_6, MoS_2, BBM-1, BBM-2, BBM-3, and BBM-4.

The value of n depends on the type of electronic transition in the semiconductor (n values of direct/indirect transition: 1/4). According to the previous reports, the n of Bi_2WO_6 and MoS_2 is 1, and their E_g are determined by the extrapolation of Tauc linear region [28,56]. The E_g of pure Bi_2WO_6 and MoS_2 are ~2.74 and 1.30 eV, respectively (Figure 4b,c), which are close to previously reported values [30,36]. The E_g of BBM-1, BBM-2, BBM-3, and BBM-4 composites are ~1.40, 1.34, 1.15, and 1.32 eV, respectively (Figure 4d–g).

On the above basis, the valence band (VB) and conduction band (CB) edge potentials of the samples are calculated in accordance with the Mulliken atomic electronegativity theory (Equations (2) and (3), respectively) [30,51]:

$$E_{CB} + 0.5E_g = X - E^e, \quad (2)$$

$$E_{VB} = E_{CB} + E_g, \quad (3)$$

where E_g and X represent the band gap energy and absolute electronegativity, respectively. E_{VB} and E_{CB} are the VB and CB edge, respectively. E^e is energy of free electrons (~4.5 eV) on the hydrogen scale. Table 1 shows the calculation results of material-related parameters. The flat-band potentials of the related materials are studied by using Mott–Schottky curves (Figure S5) to verify the rationality of the calculation results. As presented in Figure S5a–c, Bi_2WO_6 is classified as an n-type semiconductor due to its positive slope, whereas Bi_2S_3 and MoS_2 are confirmed as p-type semiconductors due to their negative slopes. When they are coupled to each other to form a n-p heterojunction ($Bi_2WO_6/Bi_2S_3/MoS_2$), the Mott–Schottky curve shows an inverted 'V-shape' characteristic (Figure S5d). Generally, E_{VB} for p-type semiconductors is very close to the flat-band potential, whereas E_{CB} for n-type semiconductors is very close to the flat-band potential [57]. The flat-band potential in the n-type semiconductor is 0.1–0.3 eV higher than E_{CB}, whereas that in the p-type semiconductor is 0.1–0.3 eV lower than E_{VB} [58]. Figure S5a–c shows that the flat-band potentials of pure Bi_2WO_6, Bi_2S_3, and MoS_2 can be confirmed to be 0.20 (0.40 eV vs. normal hydrogen electrode (NHE)), 1.06 (1.26 eV vs. NHE), and 1.14 (1.34 eV vs. NHE), respectively. Therefore, E_{CB} of pure Bi_2WO_6 and E_{VB} of Bi_2S_3 and MoS_2 can be estimated to be 0.33, 1.37, and 1.47 eV. On the basis of Equation (3), the corresponding E_{VB} of Bi_2WO_6 and E_{CB} of Bi_2S_3 and MoS_2 can occur at approximately 3.07, 0.18, and 0.17 eV. These results are in agreement with the result calculated in accordance with Mulliken atomic electronegativity theory.

Table 1. Summary of the band gap energy (E_g), conduction band edge (E_{CB}), and valence band edge (E_{VB}) of Bi_2WO_6, Bi_2S_3, and MoS_2.

Materials	E_g (eV)	X (eV)	E_e (eV)	E_{CB} vs. NHE [1] (eV)	E_{VB} vs. NHE [1] (eV)
Bi_2WO_6	2.74	6.20	4.50	0.33	3.07
Bi_2S_3	1.19 [51]	5.27	4.50	0.18	1.37
MoS_2	1.30	5.32	4.50	0.17	1.47

[1] NHE: normal hydrogen electrode.

3.6. Photoelectrochemical Performance

The catalyst is further characterized by PL spectroscopy and photocurrent response to explore its charge separation efficiency. High PL intensity indicates low charge separation efficiency and easy electron-hole recombination, whereas the photocurrent response shows the opposite [35,59,60]. The PL spectra (Figure 5a) of Bi_2WO_6 and $Bi_2WO_6/Bi_2S_3/MoS_2$ composites are obtained under the condition of $\lambda_{excitation}$ = 300 nm. The emission intensities of all $Bi_2WO_6/Bi_2S_3/MoS_2$ composites are significantly lower than that of bare Bi_2WO_6. Based on the intensity, the composites can be sorted as Bi_2WO_6 > BBM-1 > BBM-2 > BBM-4 > BBM-3. This result shows that the successful recombination of MoS_2, Bi_2S_3, and Bi_2WO_6 improves the efficiency of charge separation. The photocurrent response (Figure S6) confirms this conclusion. In the experimental process of up to 400 s, BBM-3 consistently shows the highest photocurrent. The EIS test can be used to explore the interface charge transfer properties, with the small arc radius reflecting a fast charge transfer speed [61]. Figure 5b shows the

Nyquist plots of Bi_2WO_6 and composites. The composites exhibit a smaller Nyquist plot semicircle radius compared with pure Bi_2WO_6. BBM-3 also shows a considerably smaller semicircle radius of EIS Nyquist plots than the other composites (BBM-1, BBM-2, and BBM-4), which is highly consistent with the PL and photocurrent test analysis results. Therefore, the following conclusions can be drawn. First, the construction of Bi_2WO_6, Bi_2S_3, and MoS_2 heterostructures can significantly improve the charge separation efficiency. Second, only when Bi_2WO_6 is compounded with suitable amount of Bi_2S_3 and MoS_2 can n-p heterojunction photocatalysts be formed effectively. Thus, extremely high and extremely low compounding ratios are not conducive to the formation of heterostructures and the separation and transfer of photogenerated carriers. Third, BBM-3 is expected to have the best vis-light catalytic activity because it enables the effective separation of photo-generated carriers.

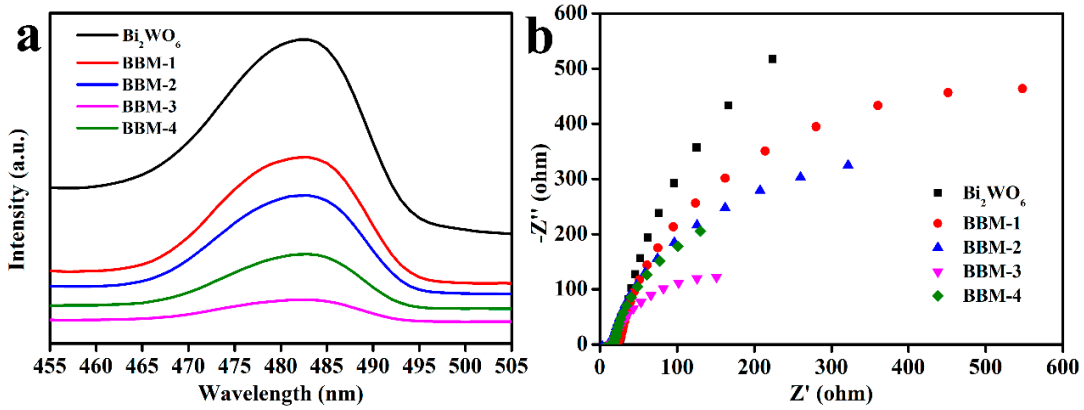

Figure 5. (**a**) Photoluminescence spectra ($\lambda_{excitation}$ = 300 nm) and (**b**) electrochemical impedance spectra (EIS) spectra of the Bi_2WO_6, BBM-1, BBM-2, BBM-3, and BBM-4.

3.7. Photocatalytic Activity

In this working system, the catalytic reduction of Cr(VI) under vis-light irradiation is used as the evaluation standard to evaluate the performance of the prefabricated materials. Previous reports have shown that the initial solution pH strongly influences the photocatalytic Cr(VI) reduction. Therefore, the pH of the initial solution is adjusted to show a linear gradient change, which is used to investigate the effect of pH on the catalytic activity of BBM-3. The photocatalytic reduction efficiency of BBM-3 is the highest under acidic conditions (Figure 6a). Under the condition of pH = 2.00, the Cr(VI) reduction rate of BBM-3 is as high as 100%. With the increase in pH, the reduction rate of Cr(VI) shows a strictly decreasing trend. When pH = 10.00, the reduction efficiency of Cr(VI) reaches 14%. This change is confirmed by the corresponding UV–vis absorption spectra (Figure 6b–d and Figure S7). The above situation is mainly caused by the following factors. First, Cr(VI) mainly exists in the form of $HCrO_4^-$ and $Cr_2O_7^{2-}$ in acidic environments and CrO_4^{2-} in alkaline environments [62]. When the solution environment is strongly acidic, the hydroxyl groups on the surface of the catalyst will be protonated to become ($-OH_2^+$), which in turn enhances the electrostatic adsorption on Cr(VI) [61]. Second, the reactions in acidic conditions are as follows (Equations (4) and (5)) [17,61,63]:

$$HCrO_4^- + 7H^+ + 3e^- \rightarrow Cr^{3+} + 4H_2O, \quad (4)$$

$$Cr_2O_7^{2-} + 14H^+ + 6e^- \rightarrow 2Cr^{3+} + 7H_2O, \quad (5)$$

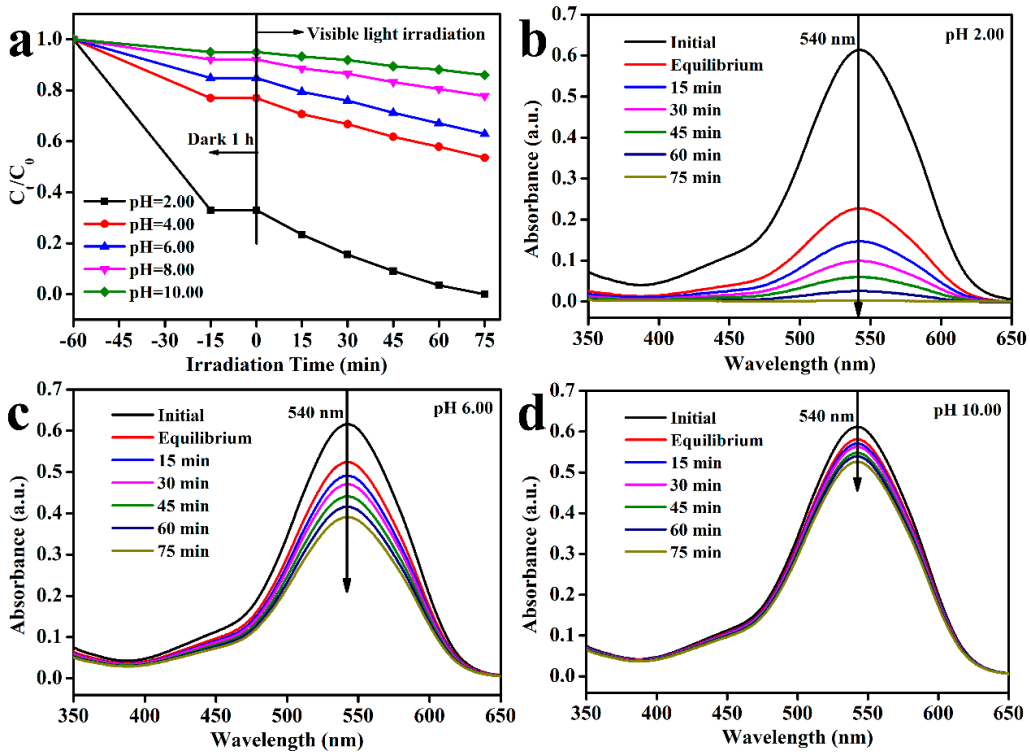

Figure 6. (**a**) Effect of pH on the catalytic activity of BBM-3. At the pH of 2.00, 6.00, and 10.00 (**b**–**d**, respectively), the UV–vis absorption spectra of Cr(VI) solution on BBM-3 sample changed.

The reaction under alkaline conditions is as follows (Equation (6)) [17,61,63]:

$$CrO_4^{2-} + 4H_2O + 3e^- \rightarrow Cr(OH)_3 + 5OH^-, \quad (6)$$

Equation (6) shows that Cr^{3+} will be converted into $Cr(OH)_3$ and deposited on the catalyst surface under alkaline conditions, blocking the active sites that can be used for adsorption and photocatalytic reactions. In summary, acidic conditions are more conducive to the reduction of Cr(VI) than alkaline conditions.

The photocatalytic activities of Bi_2WO_6 and different $Bi_2WO_6/Bi_2S_3/MoS_2$ composites are evaluated at the initial solution pH = 2.00, and the results are shown in Figure 7a. The composites exhibit high Cr(VI) adsorption performance compared with pure Bi_2WO_6, which benefits from the high surface area and abundant mesoporous structure of the composite. After 75 min of irradiation, the reduction rate of Bi_2WO_6 to Cr(VI) is 5%. By contrast, all the $Bi_2WO_6/Bi_2S_3/MoS_2$ composites manifest remarkably high photocatalytic reduction activity under the same conditions. In particular, BBM-3 shows the best photocatalytic performance with a corresponding Cr(VI) reduction rate of up to 100%. It is not difficult to find that there is an optimal compounding ratio between Bi_2S_3, MoS_2, and Bi_2WO_6 occurs in the removal of Cr(VI). Extremely low or extremely high compounding ratio is not conducive to enhancing the photoreduction activity of $Bi_2WO_6/Bi_2S_3/MoS_2$. When the actual ratio is lower than the optimal ratio, the number of active sites used to capture carriers increases with the increase in recombination ratio, thus prolonging the carrier lifetime and then increasing the photocatalytic activity. However, when the compounding ratio is higher than the optimum, excess MoS_2 will agglomerate to disrupt the effective construction of n-p heterojunction, as confirmed by the SEM result (Figure 2e).

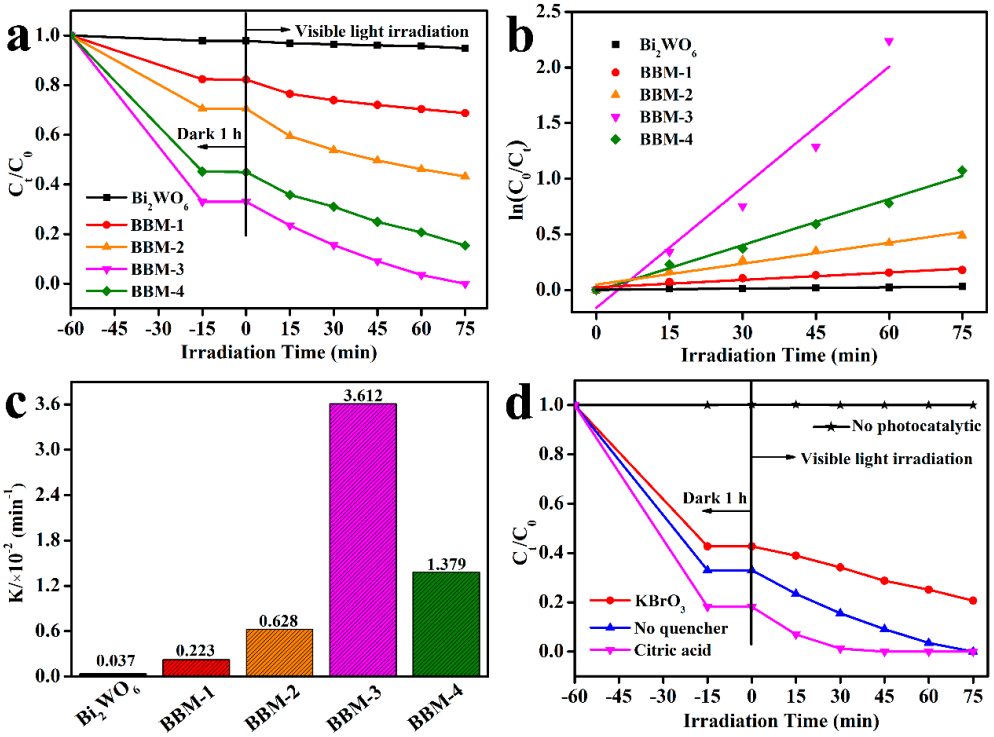

Figure 7. (**a**) Visible light (vis-light) catalytic reduction of Cr(VI) by different catalysts. (**b**) Corresponding pseudo first-order kinetic curves, and (**c**) rate constant "k" by different catalysts. (**d**) BBM-3 vis-light catalytic reduction Cr(VI) in the presence of electron scavengers ($KBrO_3$) and hole scavengers (citric acid), respectively. Dosages of $KBrO_3$ and citric acid aqueous solutions: 100 μL of 50 mg mL^{-1}.

Figure 7b shows the pseudo first-order kinetic curves of Bi_2WO_6, BBM-1, BBM-2, BBM-3, and BBM-4 for the photocatalytic reduction of Cr(VI) and the apparent reaction rate constant "*k*" (Figure 7c). The pseudo first-order model demonstrated here is shown by Equation (7) [41]:

$$ln\left(\frac{C_0}{C_t}\right) = kt, \quad (7)$$

where *t* stands for the vis-light exposure time, C_0 represents the original concentration of Cr(VI) solution, and C_t is the concentration of Cr(VI) solution at "*t*" irradiation time. The "*k*" values calculated by the linear fit of $ln(C_0/C_t)$ and irradiation time (min) plots are 0.037, 0.223, 0.628, 3.612, and 1.379 × 10^{-2} min^{-1} for Bi_2WO_6, BBM-1, BBM-2, BBM-3, and BBM-4, respectively. BBM-3 obtains the highest *k* value. Immediately afterwards, an active species capture experiment is carried out to further explore the mechanism involved in the reaction system (hole/electron trapping agent: citric acid/$KBrO_3$). The obtained results are shown in Figure 7d. First, the Cr(VI) solution without photocatalyst shows good stability under vis-light exposure. However, $KBrO_3$ significantly inhibited the photoreduction of Cr(VI) by BBM-3 with a final reduction rate of 75%. This finding indicates that the main active material in the catalytic reduction of Cr(VI) process is photogenerated electrons, which is consistent with previous reports [64]. By contrast, with the addition of citric acid, the adsorption and reduction rate of Cr(VI) by BBM-3 are significantly improved. The factors that cause this phenomenon are as follows: First, the surface of the catalyst becomes more positive by the addition of citric acid, which promotes the adsorption of $HCrO_4^-$ or $Cr_2O_7^{2-}$ ions [65]. Second, photogenerated holes can oxidize citric acid, which is equivalent to promoting the separation of photogenerated carriers and prolonging the lifetime of photogenerated electrons [61,66]. The above conclusion is confirmed by the corresponding UV–vis absorption spectra in Figure S8. Finally, compared with the other reported catalysts for vis-light reduction of Cr(VI) (Table 2), $Bi_2WO_6/Bi_2S_3/MoS_2$ heterojunction composites show relatively satisfactory photocatalytic activity.

Table 2. Performance comparison with other materials used for vis-light catalytic reduction of Cr(VI).

Materials/Amount (mg)	Cr(VI) Solution Volume (mL)/Concentration (mg L^{-1})	Time (min)	Photocatalytic Removal Rate	Publication Date	Ref.
CoS_2/g-C_3N_4-rGO/10	20/20	120	99.8	2020	[63]
$MoSe_2$/ZnO/ZnSe/80	80/20	180	100	2020	[67]
rGO/ZnO/Au/50	50/10	40	97	2020	[68]
Bi_2MoO_6/ZnO/100	50/50	150	100	2019	[61]
RGO/BiOI/ZnO/100	150/10	180	92	2019	[69]
Bi_2WO_6+Oxalic/60	50/10	120	100	2018	[70]
$CuInS_2$ QDs/Bi_2WO_6/20	40/10	300	90	2018	[71]
Bi_2WO_6/MoS_2/RGO+Lactic acid/30	100/10	80	100	2016	[72]
Bi_2WO_6/Bi_2S_3/MoS_2/20	50/40	75	100		This work

Issues such as photocatalysts separation, recovery, reuse, and stability, are important in practical applications. The stability and reusability of BBM-3 after the reaction is proven by recycling and reusing the same catalyst for three cycles. The photoreduction rate of Cr(VI) after three cycle tests is 80% (Figure 8a), which shows that the photocatalysts have enough stability and reusability. This is mainly attributed to the existence of electrostatic attraction that induces a strengthened coupling interaction among Bi_2WO_6, Bi_2S_3, and MoS_2; this interaction is beneficial to improving structural stability [51,52]. Figure S9 shows the UV–vis absorption spectra after the second and third cycles. Furthermore, we collected composite samples after use in three photocatalytic cycles (BBM-3-a) and further characterized them by XRD and XPS. The positions of the characteristic peaks of the samples after circulation (Figure 8b) exhibit no change compared with the initial sample. The evident signals of Bi, W, S, Mo, O, and Cr contaminants can be observed in the survey XPS curves of BBM-3-a (Figure 8c). The XPS peak of 577.1 eV in the Cr 2p spectrum (Figure 8d) belongs to Cr $2p_{3/2}$, which highly matches Cr(III) in $Cr(OH)_3$ [73]. To sum up, Bi_2WO_6/Bi_2S_3/MoS_2 heterojunction composite has high structural stability, good reusability, and can effectively reduce the toxicity of Cr(VI) to reduce it to Cr(III).

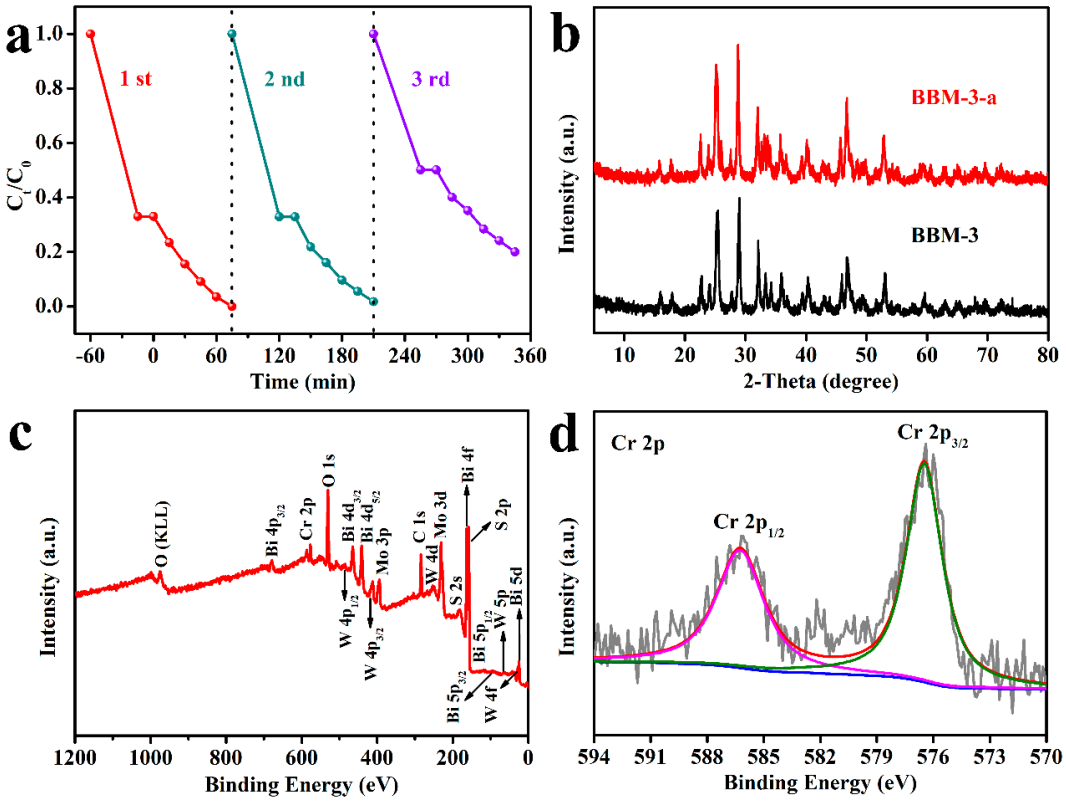

Figure 8. (**a**) Vis-light catalytic reduction of Cr(VI) by BBM-3 at different recycling runs. (**b**) XRD pattern of the BBM-3 and BBM-3-a. XPS spectra of BBM-3-a: (**c**) survey and (**d**) Cr 2p.

3.8. Possible Photocatalytic Mechanism

We can now tentatively explain the mechanism underlying heterojunctions in photocatalytic reactions. When n-type Bi_2WO_6 is coupled with p-type Bi_2S_3 and MoS_2, the n-p heterojunction is formed among semiconductors. The formation of the n-p heterojunction results in the equalization of their Fermi levels. This effect, in turn, induces band bending and a strong electric field at their interface. In this case, electrons and holes are prevented from coming into contact with each other due to the built-in electric field [74]. Meanwhile, according to the energy band structure, a type-I straddling heterojunction forms on the interface of MoS_2 and Bi_2S_3, whereas a traditional type-II staggered heterojunction forms on the interface of Bi_2S_3 and Bi_2WO_6. MoS_2 and Bi_2S_3 are excited when type-I MoS_2/Bi_2S_3 are exposed to vis-light. The electrons on the CB of MoS_2 will quickly transfer onto that of Bi_2S_3, and the holes on the VB of the MoS_2 simultaneously hop onto that of Bi_2S_3. If no measures are taken, the electrons and holes accumulate in the Bi_2S_3 semiconductor and recombine rapidly. Interestingly, the existence of type-II Bi_2S_3/Bi_2WO_6 enables the electrons on the CB of the p-type Bi_2S_3 semiconductor to transfer directly onto the CB of n-type Bi_2WO_6, and the holes on the VB of Bi_2WO_6 can be spontaneously injected into the VB of Bi_2S_3. This phenomenon realizes the effective separation and transfer of photogenerated electron-hole pairs. The strong electric field generated by the n-p heterojunction further promotes this process. Compared with a single heterostructure, this system can better realize the separation and transfer of photogenerated electron–hole pairs under the joint action of multiple heterostructures. Given the above analysis, the proposed photocatalytic reduction mechanism of Cr(VI) by $Bi_2WO_6/Bi_2S_3/MoS_2$ photocatalysis under vis-light is obtained (Scheme 2). When vis-light is irradiated on the $Bi_2WO_6/Bi_2S_3/MoS_2$ heterojunction, electrons on the semiconductor VB are excited to CB and the corresponding numbers of holes are retained on the VB, thus forming photogenerated electron–hole pairs (Equations (8)–(10)). Electrons on the CB of type-*p* Bi_2S_3 and MoS_2 are transferred to CB of type-*n* Bi_2WO_6, which is finally used for Cr(VI) reduction, whereas the holes remain in the VB of Bi_2S_3 (Equation (11)). Moreover, the CB edges of Bi_2WO_6, Bi_2S_3, and MoS_2 are more negative than the reduction potential of $E_{(Cr(VI)/Cr(III))}$ (0.51 eV) [61,67]. Theoretically, the reduction of Cr(VI) to Cr(III) can be feasibly achieved by this route. Eventually, the electrons in the system will reduce $Cr_2O_7^{2-}$ to Cr(III), and the holes will oxidize H_2O to produce O_2 (Equations (12) and (13), respectively).

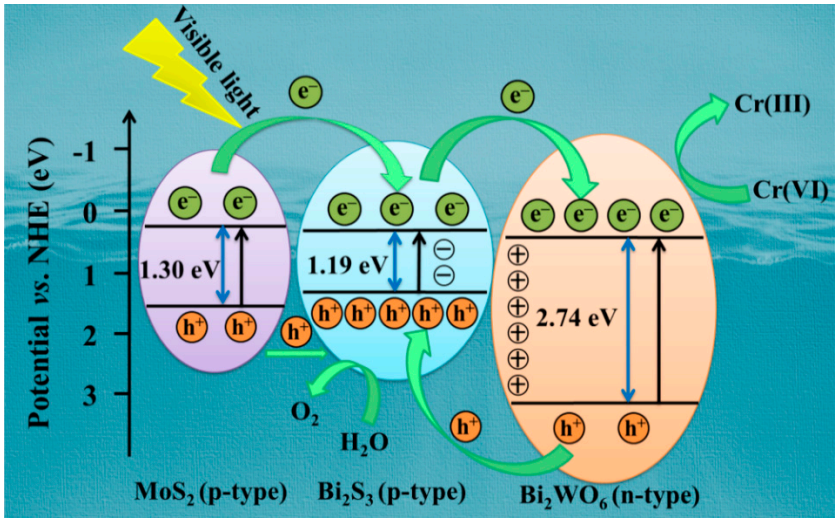

Scheme 2. Proposed photocatalytic reduction Cr(VI) mechanism of $Bi_2WO_6/Bi_2S_3/MoS_2$ under vis-light conditions.

$$Bi_2WO_6 + hv \rightarrow e^-CB + h^+VB, \quad (8)$$

$$Bi_2S_3 + hv \rightarrow e^-CB + h^+VB, \quad (9)$$

$$MoS_2 + hv \rightarrow e^-CB + h^+VB, \quad (10)$$

$$\begin{gathered} Bi_2WO_6(e^-CB) - Bi_2S_3(e^-CB) - MoS_2(e^-CB) + Bi_2WO_6(h^+VB) - Bi_2S_3(h^+VB) - MoS_2(h^+VB) \\ \rightarrow Bi_2WO_6\left({}^{total}e^-CB\right) + Bi_2S_3\left({}^{total}h^+VB\right), \end{gathered} \quad (11)$$

$$Cr_2O_7^{2-} + 14H^+ + 6e^- \rightarrow 2Cr^{3+} + 7H_2O, \quad (12)$$

$$2H_2O + 4h^+ \rightarrow O_2 + 4H^+, \quad (13)$$

4. Conclusions

In summary, spherical $Bi_2WO_6/Bi_2S_3/MoS_2$ n-p heterojunction ternary composites with vis-light response are prepared by a hydrothermal method. The HRTEM and Mott–Schottky curves confirm the formation of the n-p heterojunction. The XPS spectra show the existence of strong interaction and charge transfer among Bi_2WO_6, Bi_2S_3, and MoS_2 in the n-p heterojunction. The effects of various factors on the catalytic activity of $Bi_2WO_6/Bi_2S_3/MoS_2$ photocatalysts are investigated. For vis-light photocatalytic reduction of Cr(VI), the composites show higher photocatalytic reduction capacity than pure Bi_2WO_6, where BBM-3 exhibits the highest photocatalytic activity with a corresponding Cr(VI) reduction rate of up to 100% within 75 min. After three cycles of experiments, XRD and XPS analyses verify that the heterojunction possesses structural stability and can effectively reduce Cr(VI) into Cr(III). The improvement of photocatalytic activity of composite materials mainly benefits from the following points: First, the successful construction of a heterojunction structure forms a good interface contact, which promotes the effective separation of photogenerated electrons and holes. Second, the effective assembly and interfacial synergy between the three components enhance the vis-light absorption capacity of the samples and expand their light absorption range. Third, the increased surface area and abundant mesoporous structure endow the composites with more reactive sites and strong adsorption capacity of pollutants. The successful construction and application of $Bi_2WO_6/Bi_2S_3/MoS_2$ n-p heterojunction in this work provide new ideas and strategies for the development of photocatalysts for wastewater treatment.

Supplementary Materials: The following are available online at http://www.mdpi.com/2079-4991/10/9/1813/s1: 1. Determination of Cr(VI) concentration using the DPC method; 2. Characterization data. Figure S1: High-magnification TEM image of BBM-3, Figure S2: EDS analysis of the BBM-3, Figure S3: XPS spectra of Bi_2WO_6, Bi_2S_3, MoS_2, and BBM-3: (a) survey, (b) Mo 3d, (c) Bi 4f, and (d) W 4f spectra, Figure S4: N_2 adsorption–desorption isotherms of the Bi_2WO_6, BBM-1, BBM-2, BBM-3, and BBM-4, Figure S5: The Mott–Schottky curves of (a) Bi_2WO_6, (b) Bi_2S_3, (c) MoS_2, and (d) BBM-3, Figure S6: Photocurrent responses of Bi_2WO_6, BBM-1, BBM-2, BBM-3, and BBM-4, Figure S7: The UV–vis absorption spectra of Cr(VI) solution over the BBM-3 at (a) pH 4.00, and (b) pH 8.00, Figure S8: The UV–vis absorption spectra of Cr(VI) solution over the BBM-3 in the presence of (a) hole scavenger (citric acid) and (b) electron scavenger ($KBrO_3$), Figure S9: The UV–vis absorption spectra of Cr(VI) solution over the BBM-3 in the cycle experiments: (a) 2nd run and (b) 3rd run.

Author Contributions: Investigation, J.R., T.H., Q.G. and T.G.; Methodology, J.R., B.S. and G.Z.; Software, J.R., Q.G. and P.C.; Data curation, J.R., T.H. and Q.W.; Formal analysis, J.R., Q.G. and P.C.; Writing—original draft, J.R. and Q.G.; Visualization, J.R., Q.W., B.S. and T.G.; Writing—review and editing, B.S. and G.Z.; Conceptualization, G.Z.; Resources, G.Z.; Supervision, B.S. and G.Z.; Project administration, G.Z.; Funding acquisition, G.Z. All authors have read and agreed to the published version of the manuscript.

Funding: This research was funded by the National Natural Science Foundation of China (Grant Nos. 51972180, 51572134), Key Technology Research and Development Program of Shandong (Grant No. 2019GGX102070), and the Program for Scientific Research Innovation Team in Colleges and Universities of Jinan (Grant No. 2018GXRC006).

Conflicts of Interest: The authors declare no conflict of interest.

References

1. Cheng, C.; Chen, D.Y.; Li, N.J.; Xu, Q.F.; Li, H.; He, J.H.; Lu, J.M. $ZnIn_2S_4$ grown on nitrogen-doped hollow carbon spheres: An advanced catalyst for Cr(VI) reduction. *J. Hazard. Mater.* **2020**, *391*, 122205. [CrossRef] [PubMed]
2. Lei, C.S.; Zhu, X.F.; Zhu, B.C.; Jiang, C.J.; Le, Y.; Yu, J.G. Superb adsorption capacity of hierarchical calcined Ni/Mg/Al layered double hydroxides for Congo red and Cr(VI) ions. *J. Hazard. Mater.* **2017**, *321*, 801–811. [CrossRef]
3. Anceschi, A.; Caldera, F.; Bertasa, M.; Cecone, C.; Trotta, F.; Bracco, P.; Zanetti, M.; Malandrino, M.; Mallon, P.E.; Scalarone, D. New poly(β-Cyclodextrin)/poly(vinyl alcohol) electrospun sub-micrometric fibers and their potential application for wastewater treatments. *Nanomaterials* **2020**, *10*, 482. [CrossRef]
4. Gu, T.Y.; Dai, M.; Young, D.J.; Ren, Z.G.; Lang, J.P. Luminescent Zn(II) coordination polymers for highly selective sensing of Cr(III) and Cr(VI) in water. *Inorg. Chem.* **2017**, *56*, 4668–4678. [CrossRef]
5. Li, M.Q.; Mu, Y.; Shang, H.; Mao, C.L.; Cao, S.Y.; Ai, Z.H.; Zhang, L.Z. Phosphate modification enables high efficiency and electron selectivity of nZVI toward Cr(VI) removal. *Appl. Catal. B Environ.* **2020**, *263*, 118364. [CrossRef]
6. Pradhan, D.; Sukla, L.B.; Sawyer, M.; Rahman, P.K.S.M. Recent bioreduction of hexavalent chromium in wastewater treatment: A review. *J. Ind. Eng. Chem.* **2017**, *55*, 1–20. [CrossRef]
7. Lu, H.J.; Wang, J.K.; Hao, H.X.; Wang, T. Magnetically separable MoS_2/Fe_3O_4/nZVI nanocomposites for the treatment of wastewater containing Cr(VI) and 4-Chlorophenol. *Nanomaterials* **2017**, *7*, 303. [CrossRef]
8. Dong, R.F.; Zhong, Y.L.; Chen, D.Y.; Li, N.J.; Xu, Q.F.; Li, H.; He, J.H.; Lu, J.M. Morphology-controlled fabrication of CNT@MoS_2/SnS_2 nanotubes for promoting photocatalytic reduction of aqueous Cr(VI) under visible light. *J. Alloys Compd.* **2019**, *784*, 282–292. [CrossRef]
9. Xu, Y.L.; Chen, J.Y.; Chen, R.; Yu, P.L.; Guo, S.; Wang, X.F. Adsorption and reduction of chromium(VI) from aqueous solution using polypyrrole/calcium rectorite composite adsorbent. *Water Res.* **2019**, *160*, 148–157. [CrossRef]
10. Zheng, Y.Q.; Cheng, B.; You, W.; Yu, J.G.; Ho, W.K. 3D hierarchical graphene oxide-NiFe LDH composite with enhanced adsorption affinity to Congo red, methyl orange and Cr(VI) ions. *J. Hazard. Mater.* **2019**, *369*, 214–225. [CrossRef]
11. Zheng, X.G.; Chen, Q.; Lv, S.H.; Fu, X.J.; Wen, J.; Liu, X.H. Enhanced visible-light photocatalytic activity of Ag QDs anchored on CeO_2 nanosheets with a carbon coating. *Nanomaterials* **2019**, *9*, 1643. [CrossRef]
12. Yang, X.; Liu, L.H.; Zhang, M.Z.; Tan, W.F.; Qiu, G.H.; Zheng, L.R. Improved removal capacity of magnetite for Cr(VI) by electrochemical reduction. *J. Hazard. Mater.* **2019**, *374*, 26–34. [CrossRef]
13. Gherasim, C.V.; Bourceanu, G.; Olariu, R.I.; Arsene, C. A novel polymer inclusion membrane applied in chromium(VI) separation from aqueous solutions. *J. Hazard. Mater.* **2011**, *197*, 244–253. [CrossRef]
14. Shao, Z.C.; Huang, C.; Wu, Q.; Zhao, Y.J.; Xu, W.J.; Liu, Y.Y.; Dang, J.; Hou, H.W. Ion exchange collaborating coordination substitution: More efficient Cr(VI) removal performance of a water-stable CuII-MOF material. *J. Hazard. Mater.* **2019**, *378*, 120719. [CrossRef]
15. Yuan, X.Y.; Zhou, C.; Jing, Q.Y.; Tang, Q.; Mu, Y.H.; Du, A.K. Facile synthesis of g-C_3N_4 nanosheets/ZnO nanocomposites with enhanced photocatalytic activity in reduction of aqueous chromium(VI) under visible light. *Nanomaterials* **2016**, *6*, 173. [CrossRef]
16. Li, X.K.; Li, C.X.; Xiang, D.; Zhang, C.M.; Xia, L.; Liu, X.Y.; Zheng, F.Q.; Xie, X.Y.; Zhang, Y.L.; Chen, W. Self-limiting synthesis of Au–Pd core–shell nanocrystals with a near surface alloy and monolayer Pd shell structure and their superior catalytic activity on the conversion of hexavalent chromium. *Appl. Catal. B Environ.* **2019**, *253*, 263–270. [CrossRef]
17. Wang, Y.H.; Kang, C.L.; Xiao, K.K.; Wang, X.Y. Fabrication of Bi_2S_3/MOFs composites without noble metals for enhanced photoreduction of Cr(VI). *Sep. Purif. Technol.* **2020**, *241*, 116703. [CrossRef]
18. Huang, H.W.; Cao, R.R.; Yu, S.X.; Xu, K.; Hao, W.C.; Wang, Y.G.; Dong, F.; Zhang, T.R.; Zhang, Y.H. Single-unit-cell layer established Bi_2WO_6 3D hierarchical architectures: Efficient adsorption, photocatalysis and dye-sensitized photoelectrochemical performance. *Appl. Catal. B Environ.* **2017**, *219*, 526–537. [CrossRef]

19. Zhang, K.; Wang, J.; Jiang, W.J.; Yao, W.Q.; Yang, H.P.; Zhu, Y.F. Self-assembled perylene diimide based supramolecular heterojunction with Bi_2WO_6 for efficient visible-light-driven photocatalysis. *Appl. Catal. B Environ.* **2018**, *232*, 175–181. [CrossRef]
20. Ma, Y.C.; Lv, C.; Hou, J.H.; Yuan, S.T.; Wang, Y.R.; Xu, P.; Gao, G.; Shi, J.S. 3D hollow hierarchical structures based on 1D BiOCl nanorods intersected with 2D Bi_2WO_6 nanosheets for efficient photocatalysis under visible light. *Nanomaterials* **2019**, *9*, 322. [CrossRef]
21. Cao, R.R.; Huang, H.W.; Tian, N.; Zhang, Y.H.; Guo, Y.X.; Zhang, T.R. Novel Y doped Bi_2WO_6 photocatalyst: Hydrothermal fabrication, characterization and enhanced visible-light-driven photocatalytic activity for Rhodamine B degradation and photocurrent generatio. *Mater. Charact.* **2015**, *101*, 166–172. [CrossRef]
22. Wan, J.; Du, X.; Wang, R.M.; Liu, E.Z.; Jia, J.; Bai, X.; Hu, X.Y.; Fan, J. Mesoporous nanoplate multi-directional assembled Bi_2WO_6 for high efficient photocatalytic oxidation of NO. *Chemosphere* **2018**, *193*, 737–744. [CrossRef] [PubMed]
23. Wan, J.; Zhang, Y.; Wang, R.M.; Liu, L.; Liu, E.Z.; Fan, J.; Fu, F. Effective charge kinetics steering in surface plasmons coupled two-dimensional chemical Au/Bi_2WO_6-MoS_2 heterojunction for superior photocatalytic detoxification performance. *J. Hazard. Mater.* **2020**, *384*, 121484. [CrossRef] [PubMed]
24. Gong, Q.H.; Gao, T.T.; Hu, T.T.; Zhou, G.W. Synthesis and electrochemical energy storage applications of Micro/Nanostructured spherical materials. *Nanomaterials* **2019**, *9*, 1207. [CrossRef] [PubMed]
25. Adhikari, S.; Selvaraj, S.; Kim, D.H. Construction of heterojunction photoelectrode via atomic layer deposition of Fe_2O_3 on Bi_2WO_6 for highly efficient photoelectrochemical sensing and degradation of tetracycline. *Appl. Catal. B Environ.* **2019**, *244*, 11–24. [CrossRef]
26. Liu, X.T.; Gu, S.N.; Zhao, Y.J.; Zhou, G.W.; Li, W.J. $BiVO_4$, Bi_2WO_6, Bi_2MoO_6 photocatalysis: A brief review. *J. Mater. Sci. Technol.* **2020**, *56*, 45–68. [CrossRef]
27. Xu, Q.L.; Zhang, L.Y.; Cheng, B.; Fan, J.J.; Yu, J.G. S-Scheme heterojunction photocatalyst. *Chem* **2020**, *6*, 1543–1559. [CrossRef]
28. Xie, T.P.; Liu, Y.; Wang, H.Q.; Wu, Z.B. Layered $MoSe_2$/Bi_2WO_6 composite with P-N heterojunctions as a promising visible-light induced photocatalyst. *Appl. Surf. Sci.* **2018**, *444*, 320–329. [CrossRef]
29. Jo, W.K.; Kumar, S.; Eslava, S.; Tonda, S. Construction of Bi_2WO_6/RGO/g-C_3N_4 2D/2D/2D hybrid Z-scheme heterojunctions with large interfacial contact area for efficient charge separation and high-performance photoreduction of CO_2 and H_2O into solar fuels. *Appl. Catal. B Environ.* **2018**, *239*, 586–598. [CrossRef]
30. Meng, X.C.; Li, Z.Z.; Zeng, H.M.; Chen, J.; Zhang, Z.S. MoS_2 quantum dots-interspersed Bi_2WO_6 heterostructures for visible light-induced detoxification and disinfection. *Appl. Catal. B Environ.* **2017**, *210*, 160–172. [CrossRef]
31. Adhikari, S.; Kim, D.H. Synthesis of Bi_2S_3/Bi_2WO_6 hierarchical microstructures for enhanced visible light driven photocatalytic degradation and photoelectrochemical sensing of ofloxacin. *Chem. Eng. J.* **2018**, *354*, 692–705. [CrossRef]
32. Pan, J.B.; Liu, J.J.; Ma, H.C.; Zuo, S.L.; Khan, U.A.; Yu, Y.C.; Li, B.S. Structure of flower-like hierarchical CdS QDs/Bi/Bi_2WO_6 heterojunction with enhanced photocatalytic activity. *New J. Chem.* **2018**, *42*, 7293–7300. [CrossRef]
33. Hu, K.; Chen, C.Y.; Zhu, Y.; Zeng, G.M.; Huang, B.B.; Chen, W.Q.; Liu, S.H.; Lei, C.; Li, B.S.; Yang, Y. Ternary Z-scheme heterojunction of Bi_2WO_6 with reduced graphene oxide (rGO) and meso-tetra (4-carboxyphenyl) porphyrin (TCPP) for enhanced visible-light photocatalysis. *J. Colloid Interface Sci.* **2019**, *540*, 115–125. [CrossRef]
34. Wan, J.; Xue, P.; Wang, R.M.; Liu, L.; Liu, E.Z.; Bai, X.; Fan, J.; Hu, X.Y. Synergistic effects in simultaneous photocatalytic removal of Cr(VI) and tetracycline hydrochloride by Z-scheme Co_3O_4/Ag/Bi_2WO_6 heterojunction. *Appl. Surf. Sci.* **2019**, *483*, 677–687. [CrossRef]
35. Huang, D.L.; Li, J.; Zeng, G.M.; Xue, W.J.; Chen, S.; Li, Z.H.; Deng, R.; Yang, Y.; Cheng, M. Facile construction of hierarchical flower-like Z-scheme AgBr/Bi_2WO_6 photocatalysts for effective removal of tetracycline: Degradation pathways and mechanism. *Chem. Eng. J.* **2019**, *375*, 121991. [CrossRef]
36. Xue, W.J.; Huang, D.L.; Li, J.; Zeng, G.M.; Deng, R.; Yang, Y.; Chen, S.; Li, Z.H.; Gong, X.M.; Li, B. Assembly of AgI nanoparticles and ultrathin g-C_3N_4 nanosheets codecorated Bi_2WO_6 direct dual Z-scheme photocatalyst: An efficient, sustainable and heterogeneous catalyst with enhanced photocatalytic performance. *Chem. Eng. J.* **2019**, *373*, 1144–1157. [CrossRef]

37. Long, L.L.; Chen, J.J.; Zhang, X.; Zhang, A.Y.; Huang, Y.X.; Rong, Q.; Yu, H.Q. Layer-controlled growth of MoS_2 on self-assembled flower-like Bi_2S_3 for enhanced photocatalysis under visible light irradiation. *NPG Asia Mater.* **2016**, *8*, e263. [CrossRef]
38. Jonjana, S.; Phuruangrat, A.; Thongtem, S.; Thongtem, T. Synthesis, characterization and photocatalysis of heterostructure AgBr/Bi_2WO_6 nanocomposites. *Mater. Lett.* **2018**, *216*, 92–96. [CrossRef]
39. Babu, B.; Koutavarapu, R.; Shim, J.; Yoo, K. Enhanced solar light-driven photocatalytic degradation of tetracycline and organic pollutants by novel one-dimensional $ZnWO_4$ nanorod-decorated two-dimensional Bi_2WO_6 nanoflakes. *J. Taiwan Inst. Chem. E* **2020**, *110*, 58–70. [CrossRef]
40. Xie, J.F.; Zhang, J.J.; Li, S.; Grote, F.; Zhang, X.D.; Zhang, H.; Wang, R.X.; Lei, Y.; Pan, B.C.; Xie, Y. Controllable disorder engineering in oxygen-incorporated MoS_2 ultrathin nanosheets for efficient hydrogen evolution. *J. Am. Chem. Soc.* **2013**, *135*, 17881–17888. [CrossRef]
41. Chen, D.D.; Fang, J.Z.; Lu, S.Y.; Zhou, G.Y.; Feng, W.H.; Yang, F.; Chen, Y.; Fang, Z.Q. Fabrication of Bi modified Bi_2S_3 pillared g-C_3N_4 photocatalyst and its efficient photocatalytic reduction and oxidation performances. *Appl. Surf. Sci.* **2017**, *426*, 427–436. [CrossRef]
42. Ke, J.; Liu, J.; Sun, H.Q.; Zhang, H.Y.; Duan, X.G.; Liang, P.; Li, X.Y.; Tade, M.O.; Liu, S.M.; Wang, S.B. Facile assembly of Bi_2O_3/Bi_2S_3/MoS_2 n-p heterojunction with layered n-Bi_2O_3 and p-MoS_2 for enhanced photocatalytic water oxidation and pollutant degradation. *Appl. Catal. B Environ.* **2017**, *200*, 47–55. [CrossRef]
43. Zhou, W.J.; Yin, Z.Y.; Du, Y.P.; Huang, X.; Zeng, Z.Y.; Fan, Z.X.; Liu, H.; Wang, J.Y.; Zhang, H. Synthesis of Few-Layer MoS_2 Nanosheet-Coated TiO_2 Nanobelt Heterostructures for Enhanced Photocatalytic Activities. *Small* **2013**, *9*, 140–147. [CrossRef] [PubMed]
44. Zhu, Y.Y.; Wang, Y.J.; Ling, Q.; Zhu, Y.F. Enhancement of full-spectrum photocatalytic activity over $BiPO_4$/Bi_2WO_6 composites. *Appl. Catal. B Environ.* **2017**, *200*, 222–229. [CrossRef]
45. Chen, Y.J.; Wang, G.F.; Li, H.L.; Zhang, F.F.; Jiang, H.Y.; Tian, G.H. Controlled synthesis and exceptional photoelectrocatalytic properties of Bi_2S_3/MoS_2/Bi_2MoO_6 ternary hetero-structured porous film. *J. Colloid Interface Sci.* **2019**, *555*, 214–223. [CrossRef] [PubMed]
46. Zhou, H.M.; Xia, X.; Lv, P.F.; Zhang, J.; Pang, Z.Y.; Li, D.W.; Cai, Y.B.; Wei, Q.F. Wintersweet Branch-Like C/C@SnO_2/MoS_2 Nanofibers as High-Performance Li and Na-Ion Battery Anodes. *Part. Part. Syst. Charact.* **2017**, *34*, 1700295. [CrossRef]
47. Zhou, Y.X.; Lv, P.F.; Zhang, W.; Meng, X.D.; He, H.; Zeng, X.H.; Shen, X.S. Pristine Bi_2WO_6 and hybrid Au-Bi_2WO_6 hollow microspheres with excellent photocatalytic activities. *Appl. Surf. Sci.* **2018**, *457*, 925–932. [CrossRef]
48. Shao, B.B.; Liu, X.J.; Liu, Z.F.; Zeng, G.M.; Liang, Q.H.; Liang, C.; Cheng, Y.; Zhang, W.; Liu, Y.; Gong, S.X. A novel double Z-scheme photocatalyst Ag_3PO_4/Bi_2S_3/Bi_2O_3 with enhanced visible-light photocatalytic performance for antibiotic degradation. *Chem. Eng. J.* **2019**, *368*, 730–745. [CrossRef]
49. Song, S.S.; Wang, J.M.; Peng, T.Y.; Fu, W.L.; Zan, L. MoS_2-MoO_{3-x} hybrid cocatalyst for effectively enhanced H_2 production photoactivity of $AgIn_5S_8$ nano-octahedrons. *Appl. Catal. B Environ.* **2018**, *228*, 39–46. [CrossRef]
50. Pan, Q.C.; Zhang, Q.B.; Zheng, F.H.; Liu, Y.Z.; Li, Y.P.; Ou, X.; Xiong, X.H.; Yang, C.H.; Liu, M.L. Construction of MoS_2/C hierarchical tubular heterostructures for high-performance sodium ion batteries. *ACS Nano* **2018**, *12*, 12578–12586. [CrossRef]
51. Wang, J.Z.; Jin, J.; Wang, X.G.; Yang, S.N.; Zhao, Y.L.; Wu, Y.W.; Dong, S.Y.; Sun, J.Y.; Sun, J.H. Facile fabrication of novel $BiVO_4$/Bi_2S_3/MoS_2 n-p heterojunction with enhanced photocatalytic activities towards pollutant degradation under natural sunlight. *J. Colloid Interface Sci.* **2017**, *505*, 805–815. [CrossRef] [PubMed]
52. Cao, L.; Liang, X.H.; Ou, X.; Yang, X.F.; Li, Y.Z.; Yang, C.H.; Lin, Z.; Liu, M.L. Heterointerface engineering of hierarchical Bi_2S_3/MoS_2 with self-generated rich phase boundaries for superior sodium storage performance. *Adv. Funct. Mater.* **2020**, *30*, 1910732. [CrossRef]
53. Huang, H.W.; Zhou, C.; Jiao, X.C.; Yuan, H.F.; Zhao, J.W.; He, C.Q.; Hofkens, J.; Roeffaers, M.B.J.; Long, J.L.; Steele, J.A. Subsurface defect engineering in single-unit-cell Bi_2WO_6 monolayers boosts solar-driven photocatalytic performance. *ACS Catal.* **2020**, *10*, 1439–1443. [CrossRef]
54. Qian, X.F.; Yue, D.T.; Tian, Z.Y.; Reng, M.; Zhu, Y.; Kan, M.; Zhang, T.Y.; Zhao, Y.X. Carbon quantum dots decorated Bi_2WO_6 nanocomposite with enhanced photocatalytic oxidation activity for VOCs. *Appl. Catal. B Environ.* **2016**, *193*, 16–21. [CrossRef]

55. Song, N.N.; Zhang, M.H.; Zhou, H.; Li, C.Y.; Liu, G.; Zhong, S.; Zhang, S.Y. Synthesis and properties of Bi_2WO_6 coupled with SnO_2 nano-microspheres for improved photocatalytic reduction of Cr^{6+} under visible light irradiation. *Appl. Surf. Sci.* **2019**, *495*, 143551. [CrossRef]
56. Bai, X.; Du, Y.Y.; Hu, X.Y.; He, Y.D.; He, C.L.; Liu, E.Z.; Fan, J. Synergy removal of Cr(VI) and organic pollutants over RP-MoS_2/rGO photocatalyst. *Appl. Catal. B Environ.* **2018**, *239*, 204–213. [CrossRef]
57. Zheng, J.H.; Zhang, L. Incorporation of CoO nanoparticles in 3D marigold flower-like hierarchical architecture $MnCo_2O_4$ for highly boosting solar light photo-oxidation and reduction ability. *Appl. Catal. B Environ.* **2018**, *237*, 1–8. [CrossRef]
58. Yang, L.J.; Hu, Y.D.; Zhang, L. Architecting Z-scheme Bi_2S_3@CoO with 3D chrysanthemums-like architecture for both photoeletro-oxidization and -reduction performance under visible light. *Chem. Eng. J.* **2019**, *378*, 122092. [CrossRef]
59. Babu, B.; Koutavarapu, R.; Shim, J.; Yoo, K. Enhanced visible-light-driven photoelectrochemical and photocatalytic performance of Au-SnO_2 quantum dot-anchored g-C_3N_4 nanosheets. *Sep. Purif. Technol.* **2020**, *240*, 116652. [CrossRef]
60. Babu, B.; Koutavarapu, R.; Shim, J.; Yoo, K. Facile one-pot synthesis of gold/tin oxide quantum dots for visible light catalytic degradation of methylene blue: Optimization of plasmonic effect. *J. Alloys Compd.* **2020**, *812*, 152081.
61. Zhang, G.P.; Chen, D.Y.; Li, N.J.; Xu, Q.F.; Li, H.; He, J.H.; Lu, J.M. Fabrication of Bi_2MoO_6/ZnO hierarchical heterostructures with enhanced visible-light photocatalytic activity. *Appl. Catal. B Environ.* **2019**, *250*, 313–324. [CrossRef]
62. Zhang, F.; Zhang, Y.C.; Zhou, C.Q.; Yang, Z.J.; Xue, H.G.; Dionysiou, D.D. A new high efficiency visible-light photocatalyst made of SnS_2 and conjugated derivative of polyvinyl alcohol and its application to Cr(VI) reduction. *Chem. Eng. J.* **2017**, *324*, 140–153. [CrossRef]
63. Wang, Y.J.; Bao, S.Y.; Liu, Y.Q.; Yang, W.W.; Yu, Y.S.; Feng, M.; Li, K.F. Efficient photocatalytic reduction of Cr(VI) in aqueous solution over CoS_2/g-C_3N_4-rGO nanocomposites under visible light. *Appl. Surf. Sci.* **2020**, *510*, 145495. [CrossRef]
64. Alam, U.; Khan, A.; Bahnemann, D.; Muneer, M. Synthesis of Co doped $ZnWO_4$ for simultaneous oxidation of RhB and reduction of Cr(VI) under UV-light irradiation. *J. Environ. Chem. Eng.* **2018**, *6*, 4885–4898. [CrossRef]
65. Patnaik, S.; Swain, G.; Parida, K.M. Highly efficient charge transfer through a double Z-scheme mechanism by a Cu-promoted MoO_3/g-C_3N_4 hybrid nanocomposite with superior electrochemical and photocatalytic performance. *Nanoscale* **2018**, *10*, 5950–5964. [CrossRef] [PubMed]
66. Wang, X.; Li, Y.X.; Yi, X.H.; Zhao, C.; Wang, P.; Deng, J.G.; Wang, C.C. Photocatalytic Cr(VI) elimination over BUC-21/N-$K_2Ti_4O_9$ composites: Big differences in performance resulting from small differences in composition. *Chin. J. Catal.* **2021**, *42*, 259–270. [CrossRef]
67. Ren, Z.X.; Liu, X.J.; Zhuge, Z.H.; Gong, Y.Y.; Sun, C.Q. $MoSe_2$/ZnO/ZnSe hybrids for efficient Cr(VI) reduction under visible light irradiation. *Chin. J. Catal.* **2020**, *41*, 180–187. [CrossRef]
68. Xia, Y.; Gang, R.Q.; Xu, L.; Huang, S.J.; Zhou, L.X.; Wang, J. Nanorod-pillared mesoporous rGO/ZnO/Au hybrids for photocatalytic Cr(VI) reduction: Enhanced Cr(VI) adsorption and solar energy harvest. *Ceram. Int.* **2020**, *46*, 1487–1493. [CrossRef]
69. Yang, L.; Xu, C.; Wan, F.C.; He, H.H.; Gu, H.S.; Xiong, J. Synthesis of RGO/BiOI/ZnO composites with efficient photocatalytic reduction of aqueous Cr(VI) under visible-light irradiation. *Mater. Res. Bull.* **2019**, *112*, 154–158. [CrossRef]
70. Xu, F.; Chen, H.M.; Xu, C.Y.; Wu, D.P.; Gao, Z.Y.; Zhang, Q.; Jiang, K. Ultra-thin Bi_2WO_6 porous nanosheets with high lattice coherence for enhanced performance for photocatalytic reduction of Cr(VI). *J. Colloid Interface Sci.* **2018**, *525*, 97–106. [CrossRef]
71. Luo, S.; Ke, J.; Yuan, M.Q.; Zhang, Q.; Xie, P.; Deng, L.D.; Wang, S.B. CuInS quantum dots embedded in Bi_2WO_6 nanoflowers for enhanced visible light photocatalytic removal of contaminants. *Appl. Catal. B Environ.* **2018**, *221*, 215–222. [CrossRef]
72. Zhang, C.M.; Chen, G.; Li, C.M.; Sun, J.X.; Lv, C.D.; Fan, S.; Xing, W.N. In situ fabrication of Bi_2WO_6/MoS_2/RGO heterojunction with nanosized interfacial contact via confined space effect toward enhanced photocatalytic properties. *ACS Sustain. Chem. Eng.* **2016**, *4*, 5936–5942. [CrossRef]

73. Jiang, Z.K.; Chen, K.X.; Zhang, Y.C.; Wang, Y.Y.; Wang, F.; Zhang, G.S.; Dionysioue, D.D. Magnetically recoverable $MgFe_2O_4$/conjugated polyvinyl chloride derivative nanocomposite with higher visible-light photocatalytic activity for treating Cr(VI)-polluted water. *Sep. Purif. Technol.* **2020**, *236*, 116272. [CrossRef]
74. Hua, E.B.; Jin, S.; Wang, X.R.; Ni, S.; Liu, G.; Xu, X.X. Ultrathin 2D type-II p-n heterojunctions $La_2Ti_2O_7/In_2S_3$ with efficient charge separations and photocatalytic hydrogen evolution under visible light illumination. *Appl. Catal. B Environ.* **2019**, *245*, 733–742. [CrossRef]